

Iterative Off-resonance and Signal Decay Correction for Improved Multi-echo Imaging in MRI

Tobias Knopp, Holger Eggers, Hannes Dahnke, Jürgen Prestin, Julien S en egas

Abstract—Local deviations of the main field and signal decay due to transverse relaxation lead to perturbations of the Fourier encoding commonly applied in magnetic resonance imaging. Hence, images acquired with trajectories having long readout times suffer from artefacts such as blurring, geometric distortion, and intensity inhomogeneity. These effects can be corrected by means of iterative reconstruction algorithms, provided a field map and a relaxation map are available. Recently, a fast gridding-based approach to field inhomogeneity correction was proposed. In this work, this algorithm is extended to also handle the signal decay due to relaxation. It is then embedded in a novel fixed-point iteration algorithm that allows for the joint estimation of the field map, relaxation map, and echo images from a single multi-echo acquisition. This joint estimation approach enables the application of fast acquisition trajectories in multi-echo imaging experiments, such as spiral and echo planar, while avoiding artefacts in the reconstruction of the echo images, the field map, and the relaxation map. Since the method dispenses with the acquisition of a separate calibration scan, an appreciable overall reduction in scan time can be achieved. The evaluation of the proposed algorithm in simulations and in-vivo experiments shows a significant improvement in the reconstruction of the echo images and the estimation of the relaxation map, as compared to the standard case, where no correction is applied. The demonstrated rapid convergence of the fixed-point iteration algorithm together with the computational efficiency of the gridding-based reconstruction keeps the overall computation time reasonable.

Index Terms—Magnetic resonance imaging, image reconstruction, gridding, field inhomogeneity, off-resonance correction, relaxation, signal decay correction, iterative reconstruction, spiral imaging, echo planar imaging

I. INTRODUCTION

Measurement of relaxation rates in magnetic resonance imaging (MRI) is usually performed by means of multi-echo sequences [1], which allow for the acquisition of a series of images at increased echo times. The relaxation rate is then estimated by fitting voxel-wise an exponential function to the data of the echo time series. Such measurements are characterized by long repetition times (TR) and are, therefore, associated with relatively long scan times. One way to shorten the acquisition time consists of applying fast imaging techniques that reduce the number of phase encoding steps while preserving the spatial resolution. For example, echo planar imaging [2] and spiral imaging [3] have been applied

to collect data in multi-echo imaging experiments for T_2^* mapping. These trajectories acquire a larger portion of k -space at a given echo time, and have, therefore, long readout times. In that case however, additive dephasing due to off-resonance and relaxation-induced signal decay significantly perturb the Fourier encoding. Hence, images reconstructed by means of a Fourier transform, or by gridding in case of non-Cartesian trajectories, suffer from artefacts such as blurring, geometric distortion, and intensity inhomogeneity, depending on the chosen trajectory. Main field inhomogeneity may be due to susceptibility gradients occurring e.g. at the transition between air and tissue, as can be found in the vicinity of the sinus cavities in brain imaging or of the lung in liver imaging. Signal-decay artefacts are most pronounced in regions having short T_2^* values, such as some parts of the brain or the liver, and can be severe in the presence of iron-oxide contrast agents. This work proposes a new, time-efficient method to correct for off-resonance and signal decay artefacts in the reconstruction of multi-echo acquisitions and the estimation of the corresponding relaxation map.

Field inhomogeneity and signal decay generally affect acquisition techniques with long readout times, not only in multi-echo acquisitions, and several approaches have been proposed to reduce their effects. While technical solutions, such as shimming, may limit main field inhomogeneity due to system imperfections to some extent, nonlinear spatial variations of the main field due to susceptibility changes can only be mitigated in very rare situations and only for a spatially limited field of view [4]. Alternatively, suitable corrections during the reconstruction process can be applied. In these techniques, the off-resonance term is explicitly taken into account in the modeling of the encoding matrix, and the obtained linear system is inverted [5]. This approach can be extended to include also the signal decay due to transverse relaxation [6], [7]. These correction schemes require, however, the knowledge of both a field map and a relaxation map, which usually need to be measured in a calibration scan. A field map can be measured by acquiring two images at different echo times and dividing their phase difference by the difference in echo times. The echo spacing should be kept small to avoid wrapping errors.

Two practical issues may limit the applicability of an improved correction scheme based on pre-measured maps: the substantial scan time involved in acquiring additional data and the possible temporal variation of the field map and the relaxation map, e.g. due to physiological effects [8], between the calibration and the diagnostic scans. In the particular case of multi-echo imaging, however, data from different echo

T. Knopp is with the Institute of Medical Engineering, University of L ubeck, L ubeck, Germany (e-mail: knopp@imt.uni-luebeck.de).

H. Eggers, H. Dahnke, J. S en egas are with Philips Research Europe, Sector Medical Imaging Systems, Hamburg, Germany (e-mail: holger.eggers@philips.com, hannes.dahnke@philips.com, julien.senegas@philips.com).

J. Prestin is with the Institute of Mathematics, University of L ubeck, L ubeck, Germany (e-mail: prestin@math.uni-luebeck.de).

times are inherently acquired. Therefore, it becomes possible and attractive to jointly estimate all required quantities, i.e. the magnetization image, field map, and relaxation map, with the goal to obtain artefact-free images and maps in one step. With such a joint estimation approach, the two aforementioned problems can be circumvented.

The joint estimation of the magnetization image, field map, and relaxation map has been proposed as general reconstruction approach in [9] for fMRI, and demonstrated on simulation experiments with a rosette trajectory. The reconstruction problem to be solved is nonlinear and has a high dimensionality, therefore requiring appropriate, fast algorithms to be developed. In [10], an iterative reconstruction procedure was described for the joint estimation of magnetization image and field map on the basis of a spiral-in / spiral-out dual-echo data acquisition. As in [9], the quadratic differences between the data and the model are iteratively minimized, and a tailored minimization scheme is presented, where the magnetization image and field map are iteratively updated. It is shown that each image update can be efficiently performed by means of a fast off-resonance correction algorithm described in [11], while the field map update proceeds by gradient descent. The resulting algorithm converges relatively rapidly provided a good initial estimate of the field map can be given. In this work, we propose to extend this approach by including the relaxation rate into the correction scheme, and develop an efficient iterative algorithm for the solution of the joint estimation problem, based on a fixed-point iteration which dispenses with gradient descent techniques. The computational efficiency of the reconstruction is further improved by using a new correction algorithm, which generalizes the gridding-based algorithm, originally introduced in [12] for off-resonance correction only, in order to also correct for relaxation-induced signal decay.

We start with a mathematical description of the joint estimation of the magnetization image, field map, and relaxation map in a multi-echo imaging experiment. Then, the proposed algorithm for off-resonance and signal decay correction with given field map and relaxation map is introduced. After briefly describing a method for simultaneous field map and relaxation map estimation in image space, we present the details of the fixed-point iteration algorithm. The joint estimation method is finally evaluated in simulations and in-vivo experiments.

II. THEORY

In MRI, the relation between the demodulated signal $s_\tau(t)$ at a time point t and the transverse magnetization $m_\tau(\mathbf{r})$ at an echo time τ can be modeled by

$$s_\tau(t) = \int_{\mathbb{R}^d} m_\tau(\mathbf{r}) e^{-i\mathbf{k}(t) \cdot \mathbf{r}} d\mathbf{r}, \quad (1)$$

where $\mathbf{k}(t)$ denotes the k -space trajectory and \mathbf{r} denotes the spatial position. The phase and amplitude of the magnetization at echo time τ are mainly governed by the local angular off-resonance frequency $\omega(\mathbf{r})$, which is proportional to the local main field inhomogeneity, and the local transverse relaxation rate $R(\mathbf{r})$ according to

$$m_\tau(\mathbf{r}) = m(\mathbf{r}) e^{-i\omega(\mathbf{r})\tau} e^{-R(\mathbf{r})\tau}, \quad (2)$$

where m denotes the initial transverse magnetization. For short readout times, the model of (1) is accurate enough and, therefore, widely used in standard MR reconstruction methods. However, for longer readout times, the effects of main field inhomogeneity and relaxation cannot be neglected anymore during acquisition of the signal $s_\tau(t)$. Taking both effects into account, the model of (1) can be extended to

$$s_\tau(t) = \int_{\mathbb{R}^d} m_\tau(\mathbf{r}) e^{-i\omega(\mathbf{r})t} e^{-R(\mathbf{r})t} e^{-i\mathbf{k}(t) \cdot \mathbf{r}} d\mathbf{r}. \quad (3)$$

Both off-resonance and relaxation terms can be modeled by a single complex correction term

$$z(\mathbf{r}) := R(\mathbf{r}) + i\omega(\mathbf{r}). \quad (4)$$

In the following, we derive a discrete model by applying the rectangular rule to the integral in (3) on N equispaced voxel positions $\mathbf{r}_\rho \in [-\frac{N_1}{2}, \frac{N_1}{2}] \times \dots \times [-\frac{N_d}{2}, \frac{N_d}{2}]$. By sampling the signal $s_\tau(t)$ and the k -space trajectory $\mathbf{k}(t) \in [-\pi, \pi]^d$ at M time points t_j , we obtain

$$s_{\tau,j} \approx \sum_{\rho=0}^{N-1} m_{\tau,\rho} e^{-t_j z_\rho} e^{-i\mathbf{k}_j \cdot \mathbf{r}_\rho}, \quad (5)$$

with $s_{\tau,j} := s_\tau(t_j)$, $m_{\tau,\rho} := m_\tau(\mathbf{r}_\rho)$, $z_\rho := z(\mathbf{r}_\rho)$, and $\mathbf{k}_j := \mathbf{k}(t_j)$. Denoting moreover $m_\rho := m(\mathbf{r}_\rho)$, we can define the vectors

$$\begin{aligned} \mathbf{s}_\tau &:= (s_{\tau,j})_{j=0,\dots,M-1}, \\ \mathbf{m}_\tau &:= (m_{\tau,\rho})_{\rho=0,\dots,N-1}, \\ \mathbf{m} &:= (m_\rho)_{\rho=0,\dots,N-1}, \\ \mathbf{z} &:= (z_\rho)_{\rho=0,\dots,N-1}, \end{aligned}$$

and the matrices

$$\begin{aligned} \mathbf{H}_z &:= (e^{-t_j z_\rho} e^{-i\mathbf{k}_j \cdot \mathbf{r}_\rho})_{j=0,\dots,M-1; \rho=0,\dots,N-1}, \\ \mathbf{P}_{\tau z} &:= \text{diag}((e^{-\tau z_\rho})_{\rho=0,\dots,N-1}), \end{aligned}$$

and write (5) and (2) in matrix-vector form

$$\mathbf{s}_\tau \approx \mathbf{H}_z \mathbf{m}_\tau, \quad (6)$$

$$\mathbf{m}_\tau = \mathbf{P}_{\tau z} \mathbf{m}. \quad (7)$$

In the following, \mathbf{m}_τ will be referred to as echo image, \mathbf{m} as image, ω as field map, and R as relaxation map.

III. RECONSTRUCTION WITH KNOWN FIELD MAP AND RELAXATION MAP

A. Iterative reconstruction

First we address the problem of reconstructing an image of the magnetization given the signal \mathbf{s}_τ and the correction term \mathbf{z} . We consider the weighted least-squares problem

$$\|\mathbf{s}_\tau - \mathbf{H}_z \mathbf{m}_\tau\|_{\mathbf{W}}^2 \xrightarrow{\mathbf{m}_\tau} \min \quad (8)$$

with $\mathbf{W} := \text{diag}((w_j)_{j=0}^{M-1})$. The matrix \mathbf{W} can be used to compensate for irregular sampling in k -space. The solution of problem (8) can be computed by solving the weighted normal equation of first kind

$$\mathbf{H}_z^H \mathbf{W} \mathbf{H}_z \mathbf{m}_\tau = \mathbf{H}_z^H \mathbf{W} \mathbf{s}_\tau. \quad (9)$$

Because of the size of this linear system, we solve it iteratively with the Conjugate Gradient Normal Equation Residual (CGNR) method [13], which is a special variant of the conjugate gradient method [14] applied to the normal equation of first kind. The computational complexity of solving (9) depends on the number of iterations needed to achieve convergence and on the computational effort per iteration. The number of iterations depends mainly on the choice of the start vector and on the condition of the system matrix $\mathbf{H}_z^H \mathbf{W} \mathbf{H}_z$. For simplicity, we take the zero vector as start vector. The weights \mathbf{W} may cause a loss of signal-to-noise ratio (SNR) in theory [11], but improve the condition of the system matrix $\mathbf{H}_z^H \mathbf{W} \mathbf{H}_z$. In the simple case, where the correction term z is zero, the CGNR method has been shown to converge rapidly when using suitable density weights, usually after one iteration [15]. When z is imaginary and, therefore, contains only the field map, the system matrix remains very well conditioned, yielding rapid convergence [12]. For general complex z , the exponential decay due to the relaxation term impairs the condition of the matrix $\mathbf{H}_z^H \mathbf{W} \mathbf{H}_z$. Since this leads to noise amplification, regularization may be applied to (9).

The computational effort of one CGNR iteration depends mainly on the matrix-vector multiplications with \mathbf{H}_z and its adjoint. When $z = 0$, the complexity of one multiplication can be reduced from $\mathcal{O}(MN)$ to $\mathcal{O}(N \log N + M)$ by applying nonuniform fast Fourier transforms (NFFT) [16]. It is shown hereafter how the NFFT can be applied to reduce the complexity in the general case where $z \neq 0$.

B. Fast matrix-vector multiplication

In the expression (5), the exponential term $e^{-t_j z_\rho}$ prohibits the direct use of NFFT methods. To derive a fast algorithm for the multiplication of a vector with the matrix \mathbf{H}_z , several methods have been proposed [5], [11], [12]. All these methods can be translated into a common framework described in [17] that makes use of an approximation of the form

$$e^{-t_j z_\rho} \approx \sum_{\kappa=0}^{K-1} a_{j,\kappa} c_{\kappa,\rho} \quad (10)$$

with suitable coefficients $a_{j,\kappa}$ and $c_{\kappa,\rho}$. Inserting (10) into (5) leads to

$$s_{\tau,j} \approx \sum_{\kappa=0}^{K-1} a_{j,\kappa} \sum_{\rho=0}^{N-1} m_{\tau,\rho} c_{\kappa,\rho} e^{-i\mathbf{k}_j \cdot \mathbf{r}_\rho}. \quad (11)$$

Thus, a fast matrix-vector multiplication with the matrix \mathbf{H}_z can be realized as follows:

- 1) Compute $m'_{\tau,\rho,\kappa} = c_{\kappa,\rho} m_{\tau,\rho}$ for $\kappa = 0, \dots, K-1$.
- 2) Evaluate $s'_{\tau,j,\kappa} = \sum_{\rho=0}^{N-1} m'_{\tau,\rho,\kappa} e^{-i\mathbf{k}_j \cdot \mathbf{r}_\rho}$ for $\kappa = 0, \dots, K-1$ by means of K NFFTs.
- 3) Compute $s_{\tau,j} = \sum_{\kappa=0}^{K-1} a_{j,\kappa} s'_{\tau,j,\kappa}$.

The total number of operations is determined by the second step, yielding a computational complexity of $\mathcal{O}(K(N \log N + M))$ operations.

For the matrix-vector multiplication with the adjoint \mathbf{H}_z^H , a similar approximation can be derived

$$\sum_{\kappa=0}^{K-1} c_{\kappa,\rho} \sum_{j=0}^{M-1} s_{\tau,j} a_{j,\kappa} e^{i\mathbf{k}_j \cdot \mathbf{r}_\rho}. \quad (12)$$

This expression can be evaluated by means of adjoint NFFTs, leading to the same complexity as the evaluation of (11). Different methods to find suitable coefficients $a_{j,\kappa}$ and $c_{\kappa,\rho}$ were described. When only the field map is taken into account, these methods set either $a_{j,\kappa}$ or $c_{\kappa,\rho}$ equal to a shifted exponential and compute the remaining coefficients using an interpolation, either by means of standard window functions [5], [17], or by minimizing a min-max criterion based on the field map values [11]. While the use of standard window functions lacks accuracy, the min-max method needs to solve a linear system of equations to determine the coefficients. The computation of these coefficients can be significantly accelerated if the min-max criterion is based on the histogram of the field map [11]. An alternative, promising approach, which avoids the computational burden of solving a linear system but achieves a comparable approximation error, was described in [12]. It is limited to the case where the term z is purely imaginary, i.e. only the field map is considered for correction. In the following, we extend this approach to the case where z is an arbitrary complex number, i.e. the relaxation term is also included in the correction.

C. Gridding-based approximation

Let a real node $v \in [-\frac{1}{2}, \frac{1}{2}]$ and a complex frequency $z \in Q := \{u \in \mathbb{C} : |u| \leq \frac{B}{2}\}$ with $B \in \mathbb{N}$ be given. We consider a suitable window function $\varphi(v)$ and its Fourier transform $\hat{\varphi}(z) \neq 0$ evaluated at the complex value z . The Fourier transform exists in the complex plane if for all $u \in \mathbb{R}$, $\varphi(\cdot)e^{iu \cdot} \in L^2(\mathbb{R}) \cap L^1(\mathbb{R})$, hence we restrict φ to that class. The gridding-based approach makes use of the following approximation

$$e^{2\pi i v z} \approx \frac{1}{\alpha B \hat{\varphi}(z)} \sum_{b=-\frac{\alpha B}{2}-\mu}^{\frac{\alpha B}{2}+\mu-1} \psi(v - \frac{b}{\alpha B}) e^{2\pi i \frac{bz}{B}} \quad (13)$$

with a real oversampling factor $\alpha > 1$. $\psi(v)$ is the truncation of the window function $\varphi(v)$ with a kernel of size 2μ .

Approximation (13) was originally proposed for imaginary z in [12]. The generalization for complex z follows in a similar manner. For several window functions φ , we obtained error bounds for the relative error of (13). Each of them can be written as

$$E \leq e^{-\mu f(\alpha)} \quad (14)$$

with a positive, monotone decreasing function f . For example, for Gaussian and B-spline window functions, we obtained an error bound of less than 10^{-3} for $\alpha = 1.75$ and $\mu = 4$. For the Kaiser-Bessel functions [18], no analytical error bound of the form (14) could be found yet. However, in numerical experiments, we have observed that they yield the best approximation amongst the tested window functions.

Next, we translate approximation (13) into the framework (10). First we choose an even integer $B \in \mathbb{N}$ such that

$$\frac{|z_\rho|t_j}{2\pi} \in \left[-\frac{B}{4}, \frac{B}{4}\right)$$

for all ρ and j , and a scaling factor T such that

$$\frac{t_j}{T} \in \left[-\frac{1}{2}, \frac{1}{2}\right)$$

for all j . Because the computational complexity grows with B , we keep it as small as possible by centering z_ρ and t_κ , which involves in both domains a multiplication with an exponential. We then obtain

$$\begin{aligned} e^{-z_\rho t_j} &= e^{2\pi i \frac{t_j}{T} \frac{iz_\rho T}{2\pi}} \\ &\approx \frac{1}{\alpha B \hat{\varphi}\left(\frac{iz_\rho T}{2\pi}\right)} \sum_{b=-\frac{\alpha B}{2}-\mu}^{\frac{\alpha B}{2}+\mu-1} \psi\left(\frac{t_j}{T} - \frac{b}{\alpha B}\right) e^{-\frac{z_\rho T b}{\alpha B}}. \end{aligned} \quad (15)$$

The expression (15) has the form of (10) with $K := \alpha B + 2\mu$ and the coefficients

$$\begin{aligned} a_{j,\kappa} &:= \psi\left(\frac{t_j}{T} - \frac{\kappa - K/2}{K - 2\mu}\right), \\ c_{\kappa,\rho} &:= \frac{1}{(K - 2\mu)\hat{\varphi}\left(\frac{iz_\rho T}{2\pi}\right)} e^{-z_\rho T \frac{\kappa - K/2}{K - 2\mu}}. \end{aligned}$$

Because ψ has bounded support, the total number of coefficients $a_{j,\kappa} \neq 0$ is less than $(2\mu+1)M$. Thus the complexity of evaluating (11) is reduced to $\mathcal{O}(KN \log N + \mu M)$ operations. We note that this reduction is only valuable for nonequispaced trajectories, since, for equispaced trajectories, equation (11) can be evaluated by FFTs in $\mathcal{O}(KN \log N)$ operations.

IV. LEAST-SQUARES ESTIMATION OF IMAGE, FIELD MAP, AND RELAXATION MAP IN IMAGE SPACE

In this section, the estimation of the image \mathbf{m} and the correction term \mathbf{z} from multi-echo images is addressed. We assume that the echo images \mathbf{m}_τ are known at L echo times. Following equation (2), we obtain the nonlinear system

$$m_{\tau_l, \rho} = m_\rho e^{-\tau_l z_\rho}, \quad l = 0, \dots, L-1. \quad (16)$$

This relation can be used to estimate the image m_ρ and the correction term z_ρ for every voxel $\rho = 0, \dots, N-1$. We propose to minimize the nonlinear cost function

$$f(m_\rho, z_\rho) := \sum_{l=0}^{L-1} (m_{\tau_l, \rho} - m_\rho e^{-\tau_l z_\rho})^2 \underset{\mathbf{m}_\rho, \mathbf{z}_\rho}{\min}. \quad (17)$$

Any nonlinear optimization method, such as the Simplex [19] or the Levenberg-Marquard [20] algorithms, can be applied for this purpose. When using only two echoes, one solution of (17) can be computed explicitly without the need for a nonlinear optimization.

The estimation of the imaginary part of z_ρ , i.e. the field map, in equation (17) is prone to wrapping errors. When using equispaced echo times $\tau_l = l\delta + \tau_0$, an infinite set $\{\omega_\rho + 2\pi \frac{\kappa}{\delta} : \kappa \in \mathbb{Z}\}$ satisfies (17). Thus, if the solution is constrained in the

interval $[-\frac{\pi}{\delta}, \frac{\pi}{\delta})$, the echo spacing δ should be kept small to estimate the field map without having to apply an unwrapping algorithm. However, when using trajectories with long readout times, δ cannot be reduced arbitrarily. In those cases, we propose to combine two multi-echo measurements with the same echo spacing, but with the first echo time of the second measurement shifted by a suitable small δ' . Hence, we obtain nonequispaced echo times where the echo spacing alternates between δ' and $\delta - \delta'$. The bandwidth of the field map is then determined by the minimal echo spacing δ' yielding $[-\frac{\pi}{\delta'}, \frac{\pi}{\delta'})$.

V. JOINT ESTIMATION OF IMAGE, FIELD MAP, AND RELAXATION MAP

We now consider the general problem of jointly estimating the image \mathbf{m} and the correction term \mathbf{z} from the data \mathbf{s}_{τ_l} of a multi-echo experiment. This problem can be addressed by minimizing the nonlinear cost function

$$g(\mathbf{m}, \mathbf{z}) := \sum_{l=0}^{L-1} \|\mathbf{s}_{\tau_l} - \mathbf{H}_z \mathbf{P}_{\tau_l} \mathbf{z} \mathbf{m}\|_W^2 \underset{\mathbf{m}, \mathbf{z}}{\min}. \quad (18)$$

Straightforward minimization of (18), e.g. by means of a gradient descent algorithm [10], is feasible, but is generally associated with relatively long computation times due to the high-dimensionality of the problem. In this work, we propose an alternative approach, that uses (6) and (7) to construct a fixed-point iteration algorithm. A prerequisite is that fully sampled k -space data are available for each echo time. If the correction term \mathbf{z} is known, the echo images \mathbf{m}_{τ_l} can be computed by solving (8) as explained in Sec. III. Moreover, when the echo images \mathbf{m}_{τ_l} are known, the correction term \mathbf{z} and the image \mathbf{m} can be estimated voxel-wise by solving (17) as shown in Sec. IV. Thus, the proposed strategy is to alternately estimate the echo images \mathbf{m}_{τ_l} and the pair (\mathbf{m}, \mathbf{z}) . Each iteration $n > 0$ of the fixed-point iteration algorithm consists of the following three steps:

- 1) The echo images $\mathbf{m}_{\tau_l}^{(n)}$ are computed from the data \mathbf{s}_{τ_l} given the current value of \mathbf{z} by the CGNR algorithm of Sec. III. Fast matrix-vector multiplications with e.g. the gridding-based approach can be applied in this step.
- 2) The correction term $\mathbf{z}^{(n)}$ is estimated from the echo images $\mathbf{m}_{\tau_l}^{(n)}$ by the least-squares algorithm described in Sec. IV.
- 3) Given the new correction term $\mathbf{z}^{(n)}$ and the new image $\mathbf{m}^{(n)}$, the new residual $r^{(n)} := g(\mathbf{m}^{(n)}, \mathbf{z}^{(n)})$ is computed. To evaluate g , the fast matrix-vector multiplications with $\mathbf{H}_{\mathbf{z}^{(n)}}$ can be used again. If $r^{(n)} > r^{(n-1)}$ or the evolution in the residual is below a tolerance ε , then the procedure is stopped and $\mathbf{z} := \mathbf{z}^{(n-1)}$ and $\mathbf{m} := \mathbf{m}^{(n-1)}$ are disbursed as final results. Otherwise, the algorithm proceeds with iteration $n+1$.

The proposed fixed-point iteration algorithm is summarized in pseudo-code in Alg. 1. The residual r is computed explicitly after each iteration to monitor the convergence of the algorithm and is used as stopping criterion. The main advantage over the methods in [10] is that the computationally demanding nonlinear minimization of g is avoided, since the correction term \mathbf{z} is estimated voxel-wise from the echo images \mathbf{m}_{τ_l} .

```

Input:  $s_{\tau_l} \in \mathbb{C}^M$ ,  $\tau_l \in \mathbb{R}$ ,  $l = 0, \dots, L-1$ 
 $k_j \in [-\frac{1}{2}, \frac{1}{2}]^2$ ,  $t_j \in \mathbb{R}$ ,  $j = 0, \dots, M-1$ 
 $\mathbf{W} = \text{diag}((w_j)_{j=0}^{M-1}) \in \mathbb{R}^{M \times M}$ ,  $\varepsilon \in \mathbb{R}$ 

set  $\mathbf{z}^0 = \mathbf{0}$ 
set  $r^0 = \infty$ 
for  $n = 1, 2, \dots$  do
  for  $l = 0, \dots, L-1$  do
    solve  $\|s_{\tau_l} - \mathbf{H}_{\mathbf{z}^{(n-1)}} \mathbf{m}_{\tau_l}^{(n)}\|_{\mathbf{W}} \xrightarrow{\mathbf{m}_{\tau_l}^{(n)}} \min$  by the
    CGNR algorithm of Sec. III
  end for
  for  $\rho = 0, \dots, N-1$  do
    solve  $\sum_{l=0}^{L-1} \left( m_{\rho, \tau_l}^{(n)} - m_{\rho}^{(n)} e^{-\tau_l z_{\rho}^{(n)}} \right)^2 \xrightarrow{m_{\rho}^{(n)}, z_{\rho}^{(n)}} \min$  by a
    nonlinear optimization algorithm (Sec. IV)
  end for
  compute  $r^{(n)} := g(\mathbf{m}^{(n)}, \mathbf{z}^{(n)})$ 
  if  $r^{(n)} > r^{(n-1)}$  or  $\frac{|r^{(n)} - r^{(n-1)}|}{2|r^{(n)} + r^{(n-1)}|} < \varepsilon$  then
    set  $\mathbf{m} = \mathbf{m}^{(n-1)}$ 
    set  $\mathbf{z} = \mathbf{z}^{(n-1)}$ 
    break
  end if
end for

Output:  $\mathbf{m} \in \mathbb{C}^N$ ,  $\mathbf{z} \in \mathbb{C}^N$ 

```

Algorithm 1: Pseudo-code of the fixed-point iteration algorithm.

In practice, a preprocessing of the correction term before multiplication with the matrix $\mathbf{H}_{\mathbf{z}}$ leads to better results. We applied a mean-shift filter [21] to each of the real and imaginary parts of the correction term. If the echo spacing δ' is too large, an additional unwrapping of the field map might be applied.

VI. METHODS

A. Simulations

The simulations were based on a Shepp-Logan phantom with a resolution of 256×256 , to which a slightly smoothed circular shutter with a radius of $\frac{7}{8}\pi$ was applied in k -space. In this way, we took into account that spiral acquisitions sample only a circular area in k -space and that field inhomogeneity leads to an additional signal modulation [12]. The main field inhomogeneity was modeled by a parabolic field map with off-resonance frequencies in the range of -125 Hz to $+125$ Hz. For the relaxation map, an unmodified Shepp-Logan phantom was scaled to fit into the range of 5 s^{-1} to 50 s^{-1} . The image, field map, and relaxation map used for the simulations are shown in Fig. 1.

To evaluate the accuracy of the gridding-based correction algorithm of Sec. III, we simulated k -space data by a direct evaluation of (5) using a spiral trajectory with 12 profiles, 6000 samples per profile and a sample interval of $10 \mu\text{s}$. Reconstruction was performed with the known field map and relaxation

map, using the proposed gridding-based correction algorithm and the min-max interpolation with time segmentation from [11] for comparison. We used Kaiser-Bessel functions as window functions for the gridding-based algorithm.

To test the least-squares method for the estimation of the image, field map, and relaxation map described in Sec. IV, we simulated multi-echo images by evaluating (2) and adding Gaussian noise with zero mean yielding a signal to noise ratio of 20. The number of echo times included in the computation varied from 2 to 32. A nonequispaced distribution of the echo times, as described in Sec. IV, was chosen, with $\delta = \frac{100}{L-1}$ ms and $\delta' = 1$ ms. Note that the number of echoes decreases when the echo spacing δ increases: this is the situation encountered in multi-echo imaging with fixed repetition time, where the minimal echo spacing is bounded by the readout time and the maximum number of echoes acquired is given by the repetition time and the echo spacing.

The algorithm for the joint estimation of the image, field map, and relaxation map was finally tested with multi-echo data. First, the performance of the fixed-point iteration algorithm was compared to that of the iterative minimization algorithm of [10]. For that purpose, a dual-echo spiral trajectory was used with 12 profiles, 6000 samples per profile, a sample interval of $10 \mu\text{s}$, a difference between the echo times of $\delta' = 1$ ms and $\tau_0 = 0$ ms. The simulation and reconstruction were performed using only the field map and, therefore, ignoring relaxation effects, in order to reproduce the situation addressed in [10]. Both algorithms used the same parameters for the image reconstruction step, which used the histogram approach described in [11]. They were initialized with the same field, which was obtained after a gridding reconstruction of the data. For the calculation of the spiral density weights, an approximative method [22] was used. Next, multi-echo EPI and spiral data were simulated with a grid size of 256×256 , a sample interval of $5 \mu\text{s}$, and $L = 12$ nonequispaced echo times with $\delta = 16$ ms, $\delta' = 1$ ms, and $\tau_0 = 0$ ms. The EPI trajectory consisted of 32 EPI trains of length 8 each. The spiral trajectory consisted of 24 profiles and 3000 samples per profile. As parameters for the gridding-based correction algorithm, $K = 26$ segments and 8 CGNR iterations were used.

All algorithms were programmed in C. The reconstruction was performed on a conventional workstation with an Intel Xeon processor running at 2 GHz and with 4 GB of memory. To quantify the accuracy of the proposed algorithms, the normalized root mean square (NRMS) error was used as measure. It was computed by taking the ratio between the Euclidean norm of the difference between estimated and original vector and the Euclidean norm of the original vector.

B. Experiments

In-vivo imaging in the brain was performed on a 1.5 T Achieva whole-body scanner (Philips Medical Systems, Best, The Netherlands). In order to test the joint estimation approach in the presence of significant field inhomogeneities, a central sagittal slice (slice thickness: 4 mm) was chosen. Multi-echo EPI data were measured with a FOV of 270 mm, an image

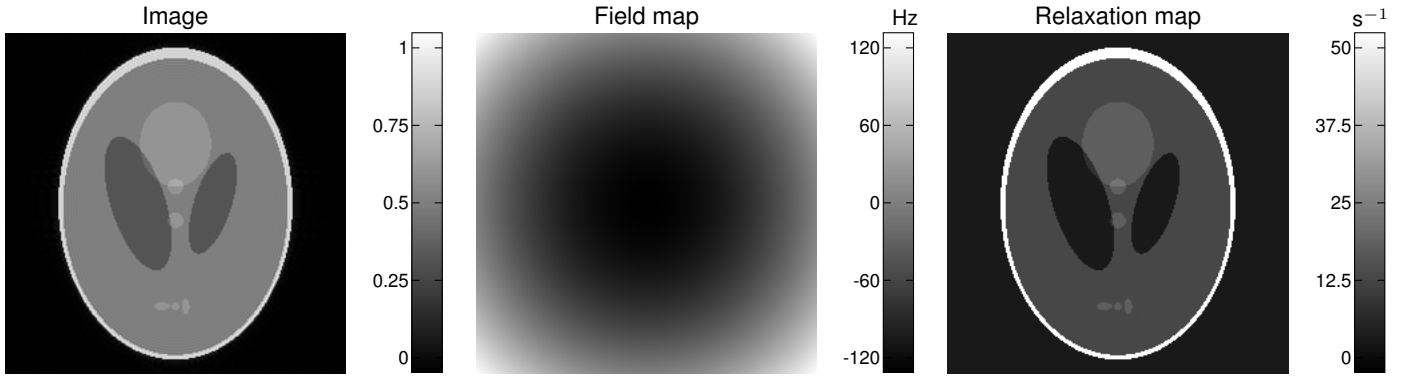


Fig. 1. Image, field map, and relaxation map used in simulations. Shown are a filtered Shepp-Logan phantom on the left, a parabolic field map with off-resonance frequencies in the range of -125 Hz to $+125$ Hz in the middle, and an unfiltered Shepp-Logan phantom as relaxation map in the range of 5 s^{-1} to 50 s^{-1} on the right.

size of 256×256 , and a repetition time of $TR=100$ ms. The EPI trajectory consisted of 28 EPI trains of length 9 each. Five echoes with an echo spacing of $\delta = 20.1$ ms were acquired after each RF pulse. Two such multi-echo EPI measurements, one with $\tau_0 = 11$ ms and the other one with $\tau_0 = 12$ ms, were combined to obtain a minimal echo spacing of $\delta' = 1$ ms. Moreover, multi-echo spiral data were measured with a FOV of 250 mm, an image size of 256×256 , and a repetition time of $TR=100$ ms. The spiral trajectory consisted of 17 profiles. 5 echoes with an echo spacing of $\delta = 20$ ms were acquired sequentially. Again, two multi-echo measurements, one with $\tau_0 = 2$ ms and the other one with $\tau_0 = 3$ ms, were combined to obtain a minimal echo spacing of $\delta' = 1$ ms.

VII. RESULTS

A. Simulations

The results of the off-resonance and signal decay correction with known field map and relaxation map for the simulated spiral data are shown in Fig. 2a, for the proposed gridding-based algorithm and for the min-max algorithm with time segmentation. The accuracies of the two algorithms were compared for different numbers of time segments K , and after 10 CGNR iterations. Since the gridding-based correction algorithm depends only indirectly on the number of segments K , we chose α and m as parameter values for the gridding-based algorithm to fit the desired K . For $\alpha = 1.25$ and $\mu = 2$, the resulting number of segments was $K = 16$. For less than 16 segments, the condition $\alpha > 1$ does not hold true anymore, and the gridding-based correction algorithm yields a poor accuracy. For more than $K = 16$ segments, both algorithms achieve similar reconstruction accuracy. Since the gridding-based algorithm does not need to solve a linear system to compute the coefficients $a_{j,\kappa}$ and $c_{\kappa,\rho}$ of (10), it is faster than the min-max interpolation for a given number of time segments K .

Moreover, in order to motivate the use of a complex correction term consisting of the field map and relaxation map in the reconstruction, we compared three correction levels for the reconstruction of the simulated spiral data: a reconstruction without correction (standard gridding reconstruction), a reconstruction where only the field map was included in the

correction, and a reconstruction with both the field map and the relaxation map included in the correction. The reconstructions with non-zero correction terms used the gridding-based algorithm with $K = 16$ segments. The results are shown in Fig. 2b. In this example, the off-resonance correction reduces the reconstruction error from 27% to 8%. When both correction terms are taken into account, the error can be reduced to 0.9%, which is a significant improvement. Interestingly, when the field map and the relaxation map are both included in the correction, the CGNR algorithm needs more iterations to converge. This behaviour can be explained by the degradation of the condition of the system matrix when the relaxation term is included.

Next, we assessed the accuracy of the nonlinear least-squares method for the estimation of the image, field map, and relaxation map in image space. The NRMS errors of the image, field map, and relaxation map are plotted as a function of the number of echo times in Fig. 3. In the setting chosen, a small echo time number corresponds to a large echo spacing. A rapid decrease of the field map and relaxation map errors can be observed as this number slightly increases. Since the time latency between two echo times can be used to sample k -space and reduce the overall acquisition time, a compromise has to be found between scan speed and precision. The estimation of the image also benefits from an increase in the number of echo times, but not in the common square root fashion, because the data at the successive echo times have decreasing SNR due to relaxation.

The comparison of the fixed-point iteration algorithm and the iterative optimization of [10] is summarized in Tab. I. The normalized residual was computed as the ratio between the residual at a given iteration and the residual at the initialization. It indicates the progress in the minimization. For both algorithms, the decrease of the residual is the largest after one iteration, and is much slower afterwards. However, after 5 iterations, the fixed-point iteration algorithm yields a significantly lower value of the normalized residual. We also observed that the convergence of the iterative optimization of [10] was sensitive to the initial field map value provided. If initialized with a zero field map, convergence was very slow. Interestingly, the decrease of the residual yields a decrease

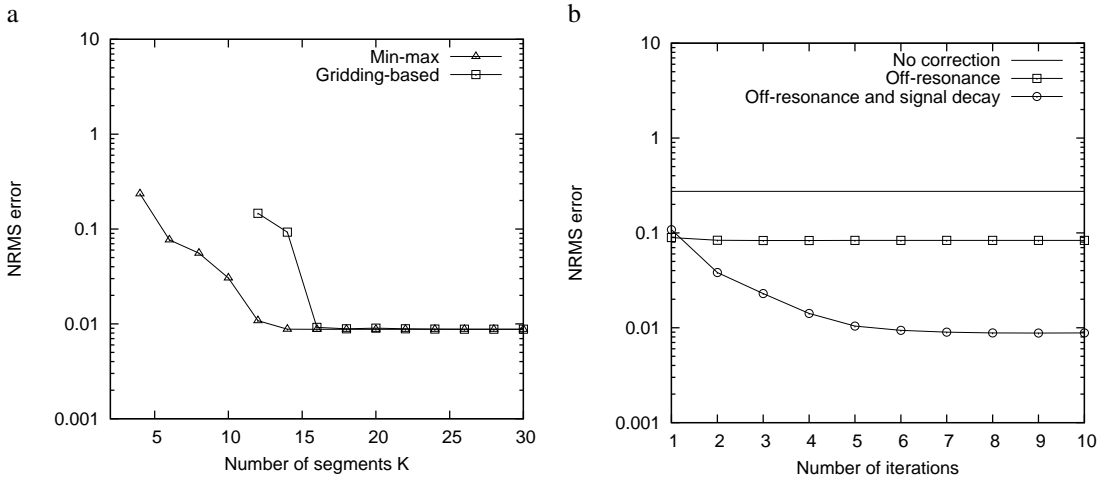


Fig. 2. Reconstruction error of different off-resonance and signal decay correction algorithms. Plotted is the normalized root mean square (NRMS) error. a: As function of the number of segments K with 10 CGNR iterations for the gridding-based and for the min-max approach. b: As function of the number of CGNR iterations for: a reconstruction with no correction, a reconstruction with correction of off-resonance only (gridding-based with $K = 16$), and a reconstruction with correction of both off-resonance and signal decay (gridding-based with $K = 16$).

TABLE I

COMPARISON OF THE FIXED-POINT ITERATION ALGORITHM AND THE ITERATIVE OPTIMIZATION ALGORITHM FOR THE JOINT ESTIMATION OF THE IMAGE AND FIELD MAP FOR A SIMULATED DUAL-ECHO SPIRAL ACQUISITION.

Algorithm	Iteration	Normalized residual	NRMS error (image)	NRMS error (field map)	Running time
Iterative optimization [10]	1	$7.3 \cdot 10^{-3}$	$2.7 \cdot 10^{-2}$	$4.9 \cdot 10^{-3}$	145 s
	5	$7.2 \cdot 10^{-3}$	$2.5 \cdot 10^{-2}$	$4.7 \cdot 10^{-3}$	470 s
Fixed-point iteration	1	$9.9 \cdot 10^{-3}$	$2.7 \cdot 10^{-2}$	$4.9 \cdot 10^{-3}$	28 s
	5	$6.9 \cdot 10^{-3}$	$1.3 \cdot 10^{-2}$	$1.4 \cdot 10^{-3}$	128 s

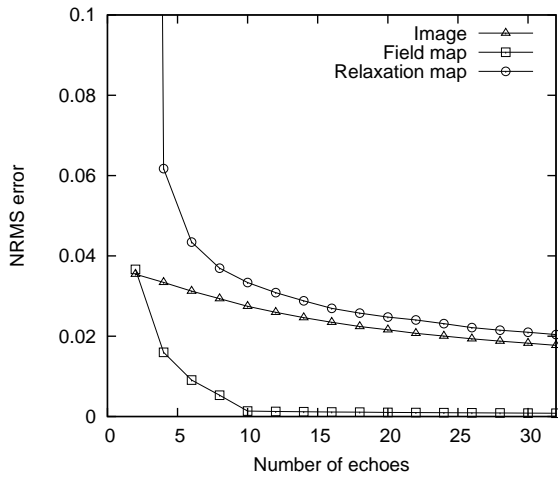


Fig. 3. Estimation error of the image, field map, and relaxation map computed by the least squares algorithm. Multi-echo images were simulated with the images shown in Fig. 1 applying normal distributed noise (SNR=20). Plotted is the normalized root mean square (NRMS) error as function of the number of echo times.

in the estimation error of the image and the field map. This suggests that monitoring this decrease is a good indicator of the convergence of the fixed-point iterative algorithm. In our implementation of the iterative optimization of [10], the running time per iteration may vary, depending of the number of steps needed to reach convergence in the gradient descent step. By comparison, the running time of one iteration of the fixed-point iteration algorithm is approximatively constant,

since the field map update is a non-iterative procedure. In summary, the proposed fixed-point algorithm converges faster, and each iteration takes less time, yielding an appreciable decrease of overall computation time in this example.

The results of the joint estimation approach for the simulated multi-echo EPI and spiral acquisitions are shown in Fig. 4. The plots depict the evolution of the NRMS errors of the reconstructed image, field map, and relaxation map as a function of the number of iterations. Figs. 5 and 6 show the corresponding images and maps obtained after one iteration and after convergence. For both types of trajectories, the fixed-point iteration algorithm converges within a few iterations. The image and maps obtained after one iteration of the proposed algorithm correspond to the standard estimates, reconstructed without correction. Once convergence is reached, the estimation errors of all quantities are reduced to a low level. Some residual blurring can be observed at the edges of the phantom in the multi-echo spiral case. This may be due to a less accurate estimation of the field map at this location, as suggested by the field map differences of Fig. 6. This blurring causes local errors in the estimation of the relaxation map, which explains the higher values in the relaxation error plot of Fig. 4. With that exception, all quantities are estimated with a precision below 2%. Interestingly, the error decreases significantly between the first iteration, which corresponds to a reconstruction with no correction, and convergence, especially for the image and the relaxation map. This demonstrates that the proposed joint estimation yields an appreciable improvement in accuracy.

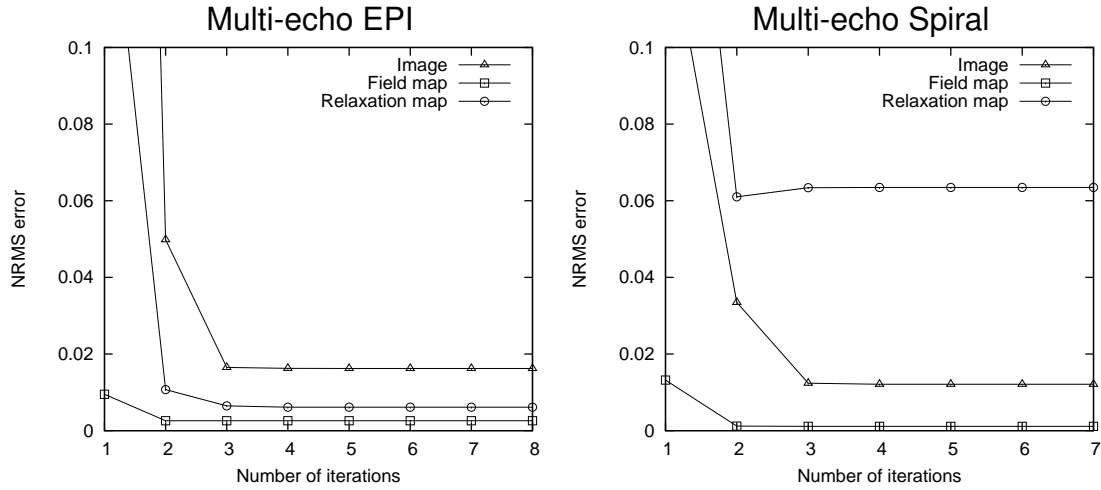


Fig. 4. Reconstruction error of the fixed-point iteration algorithm as a function of the number of iterations.

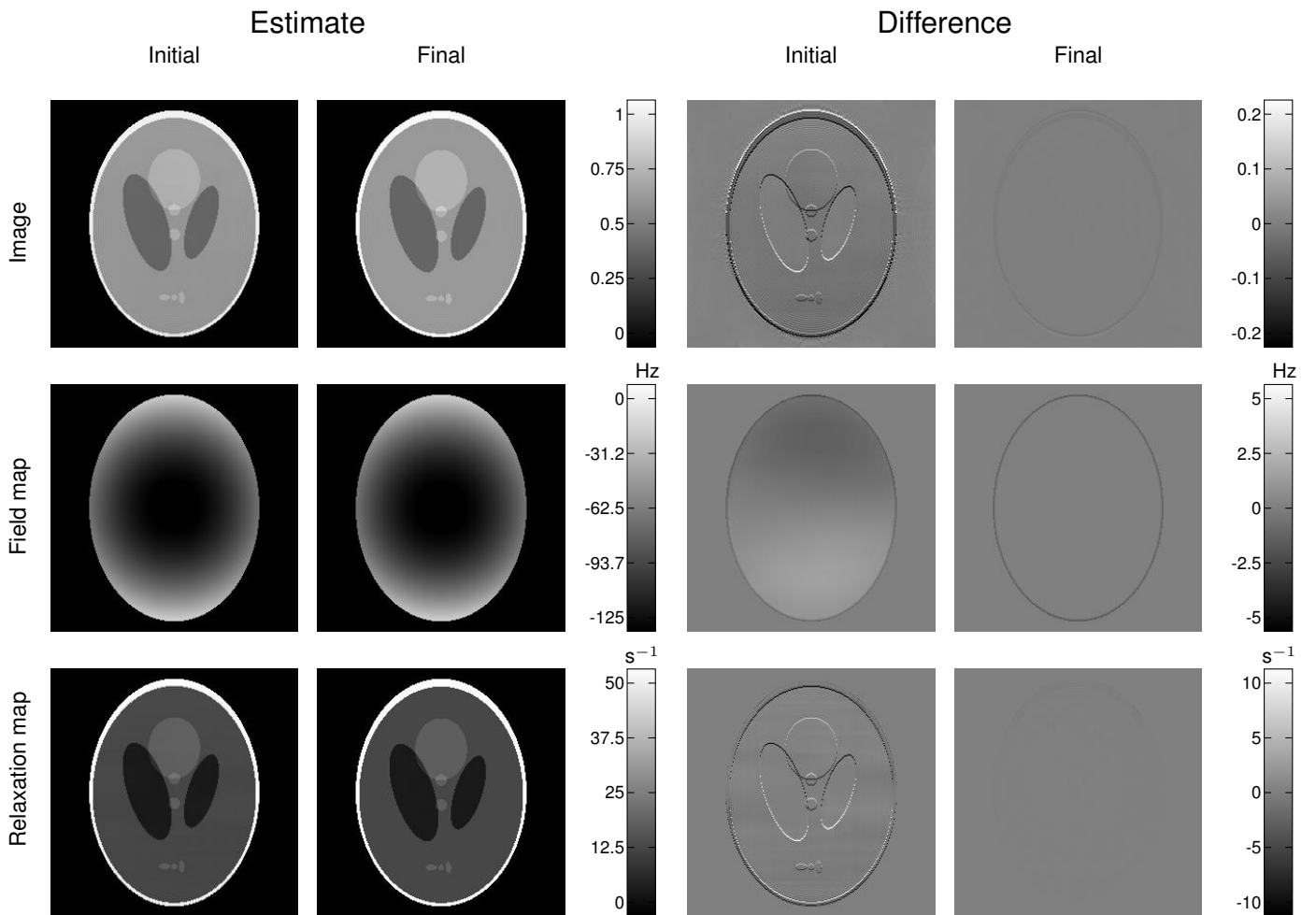


Fig. 5. Results of the fixed-point iteration algorithm for the multi-echo EPI dataset, after one iteration (Initial) and after convergence (Final). The resulting estimates are shown on the left, the difference between estimated and original quantities on the right.

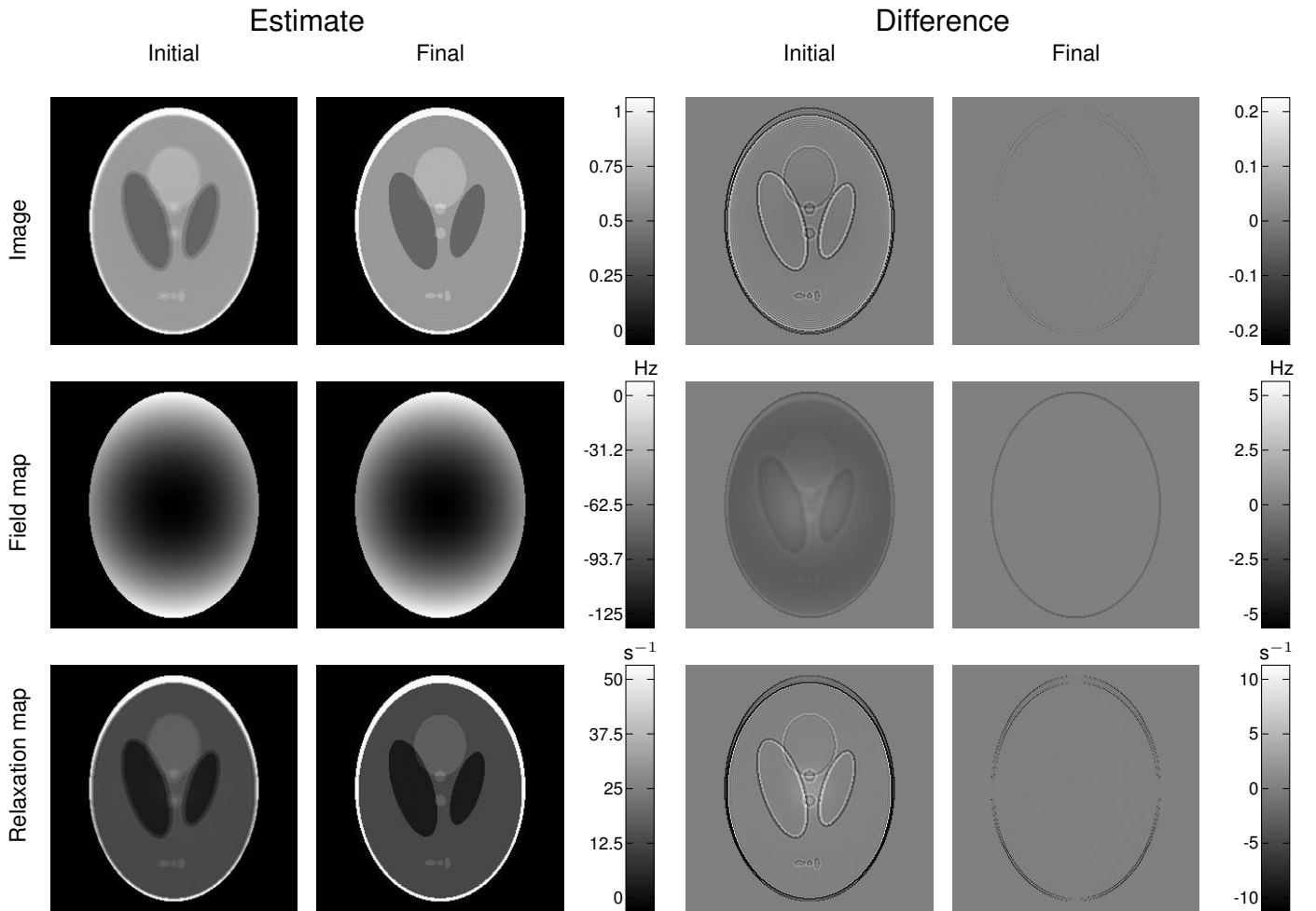


Fig. 6. Results of the fixed-point iteration algorithm for the multi-echo spiral dataset, after one iteration (Initial) and after convergence (Final). The resulting estimates are shown on the left, the difference between estimated and original quantities on the right.

B. Experiments

The results of the joint estimation approach applied to multi-echo imaging in the brain are shown in Fig. 7 for the EPI data, and in Fig. 8 for the spiral data. Significant field inhomogeneity, with off-resonance values up to 150 Hz, can be observed in the basal brain region, in the vicinity of the sinus cavities, and causes loss of spatial information in the two acquisitions. Moreover, with T_2^* values below 30 ms in some areas, signal loss larger than 50% can occur considering the long readout times of approximately 20 ms used in the experiments. Reconstruction was performed with the fixed-point iteration algorithm, which reached convergence in both cases after four iterations. For the EPI acquisition, correction of local geometric distortions of up to two voxels can be observed between the initial and the final estimates. In the spiral acquisition, the initial image and relaxation map are affected by strong blurring artefacts, which are effectively corrected after convergence of the fixed-point iteration algorithm.

VIII. DISCUSSION

Off-resonance and relaxation-induced signal decay affect the Fourier encoding in magnetic resonance imaging and cause significant artefacts for acquisitions with long readout

times. While an accurate correction of these two effects in principle requires the knowledge of both a field map and a relaxation map, we showed that a joint estimation approach of image and maps can be adopted in the case of multi-echo acquisitions. With this method, separate measurements of the field map and the relaxation map are not required, thus dispensing with time-consuming additional scans. By applying the proposed reconstruction, longer readout times can be used for data acquisition without compromising accuracy in the estimation of the image and of the relaxation map. Therefore, the proposed framework can be applied to reduce the total scan time in multi-echo imaging, as demonstrated in this work with the use of echo planar and spiral trajectories.

The use of longer readout times for data acquisition leads to an increase of the minimal echo spacing achievable between two echo times. This in turn may lead to a severe degradation of the estimation of the field map and of the relaxation map, as illustrated by the results of Fig. 3. To mitigate the wrapping errors in the estimation of the field map, we proposed to combine two distinct multi-echo acquisitions with a large echo spacing and slightly different first echo times. The resulting echo times are nonequispaced. The sampling of the echo times should also be adapted to the expected

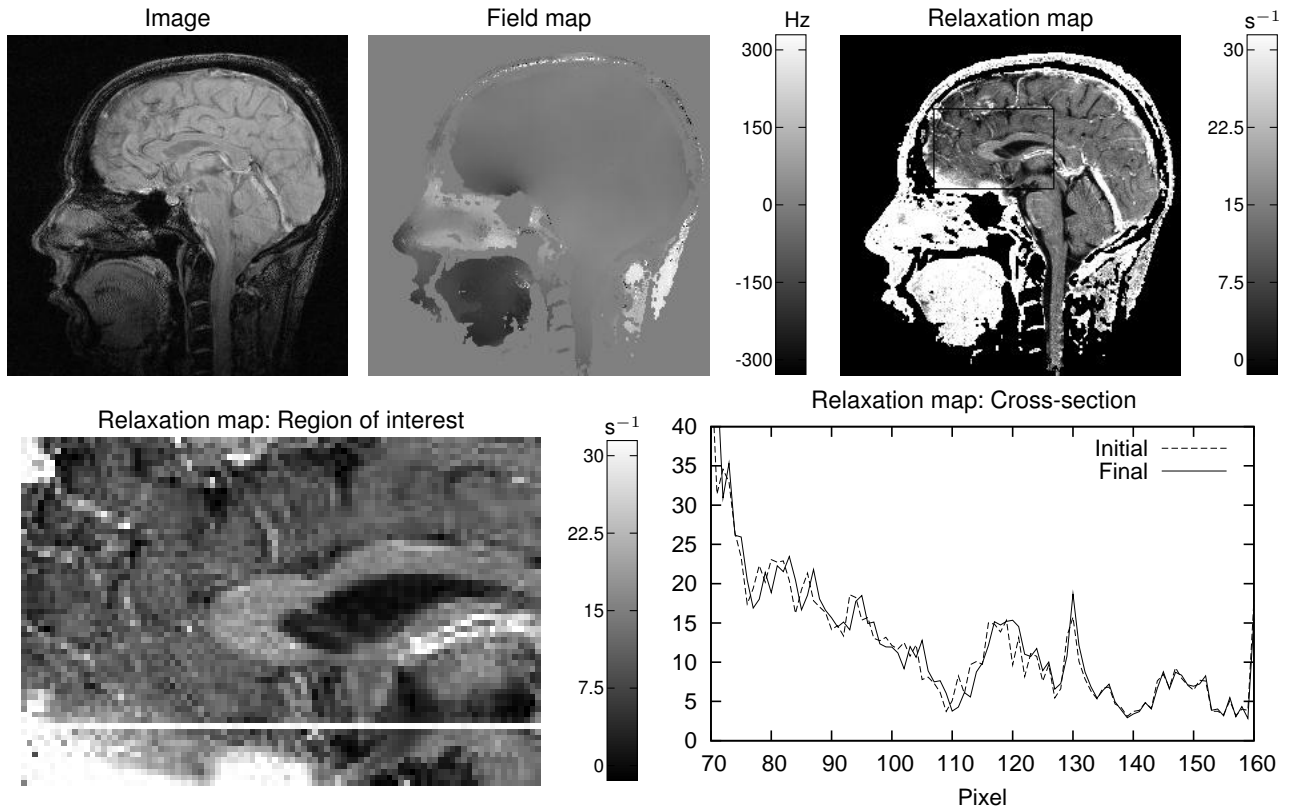


Fig. 7. Results of the fixed-point iteration algorithm for the brain multi-echo EPI dataset. Shown are the image, the field map, and the R_2^* relaxation map after convergence, an enlargement of a detail of the final R_2^* relaxation map, and a cross section of this map showing initial and final profiles.

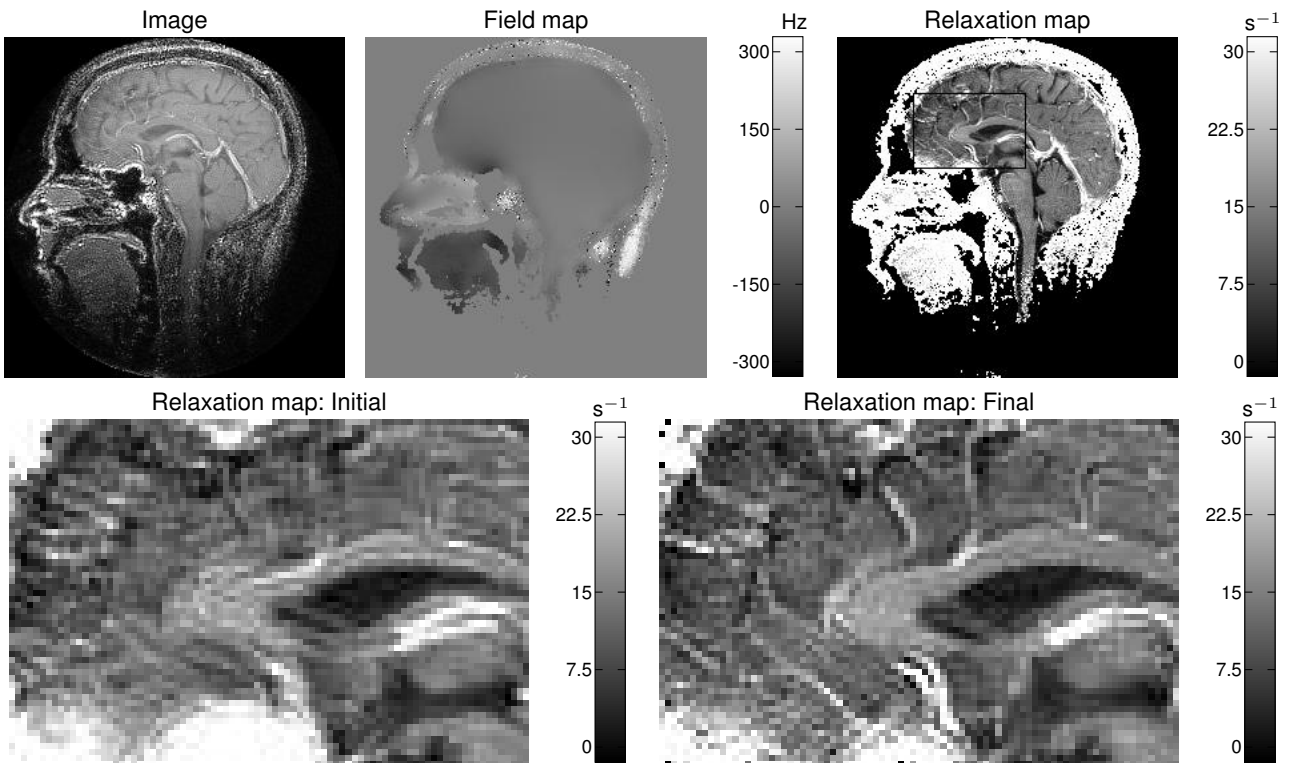


Fig. 8. Results of the fixed-point iteration algorithm for the brain multi-echo spiral dataset. Shown are the image, the field map, and the R_2^* relaxation map after convergence, and an enlargements of a detail of the initial and final R_2^* relaxation maps.

relaxation rates, and, therefore, there is a limit to the maximal readout time that can be used in practice. Even with these limitations, the simulation results show that the relaxation map can be estimated accurately with a significant reduction of scan time: for example, relaxation rates could be estimated with a precision of 1% by combining two EPI acquisitions with an echo train of length 8, resulting in a net acceleration of 4 in comparison to a standard Cartesian acquisition.

In general, the solution of a high-dimensional, nonlinear estimation problem is a complex optimization task associated with long computation times. In the special case of the joint estimation of the image, field map, and relaxation map from multi-echo data, we were able to derive an efficient computation algorithm. The central idea was to apply a fast correction algorithm to reconstruct an image at each echo time, and to perform the estimation of the field map and the relaxation map in image space, where these two quantities can be estimated voxel-wise by means of efficient nonlinear least-squares methods. The resulting fixed-point iteration algorithm was shown to converge rapidly, typically in less than 10 iterations, and did not require a good initialization of the field map and the relaxation map. In the case of dynamic experiments, for which small changes of the field map and relaxation map are expected, the proposed fixed-point iteration algorithm and the iterative minimization algorithm of [10] may perform comparably, and it is likely that the linearization approach presented in [8] yields sufficient accuracy in less computation time. However, for the case of multi-echo imaging without any prior knowledge of the field map and the relaxation map, the fixed-point iteration algorithm turns out to be more efficient in terms of running time. For the multi-echo EPI data of the in-vivo experiment, consisting of 10 echoes and an image size of 256×256 , the running time of one iteration of the fixed-point iteration algorithm was below two minutes. A limitation of this algorithm in comparison with more general optimization approaches is that it currently requires fully sampled datasets at the different echo times.

During the course of the fixed-point iterations, the reconstruction of the echo images must be repeated with different values of the field map and the relaxation map. Hence, applying the min-max algorithm with time segmentation of [11] would necessitate to compute new coefficients $a_{j,\kappa}$ and $c_{\kappa,\rho}$ in (10) at each iteration, by solving a linear system, which is computationally prohibitive. Systematic recomputation of these coefficients may be avoided if the histogram of the field map is used for the min-max criterion, since it can be argued that this one does not vary substantially from one iteration to the next. The alternative, gridding-based algorithm described in this work allows for a direct evaluation of the required coefficients by means of a suitable window function. It was shown to provide a very good accuracy provided a sufficient number of segments is used. This algorithm may find applications outside multi-echo imaging, in cases where a field map and a relaxation map are readily available.

REFERENCES

[1] E. M. Haacke, R. W. Brown, M. R. Thompson, and R. Venkatesan, *Magnetic Resonance Imaging: Physical Principles and Sequence De-*

sign. Wiley-Liss, 1999.

[2] O. Speck and J. Hennig, "Functional imaging by I_0 - and T_2^* -parameter mapping using multi-image EPI," *Magn. Reson. Med.*, vol. 40, pp. 243–248, Aug 1998.

[3] M. Barth, A. Metzler, M. K. S. Röhl, E. Moser, and D. Leibfritz, "Functional MRI of the human motor cortex using single-shot, multiple gradient-echo spiral imaging," *Magn. Reson. Imag.*, vol. 17, pp. 1239–1243, Nov 1999.

[4] K. M. Koch, P. B. Brown, D. L. Rothman, and R. A. de Graaf, "Sample-specific diamagnetic and paramagnetic passive shimming," *J. Magn. Reson.*, vol. 182, no. 1, pp. 66–74, 2006.

[5] D. Noll, C. Meyer, J. Pauly, D. Nishimura, and A. Macovski, "A homogeneity correction method for magnetic resonance imaging with time-varying gradients," *IEEE Trans. Med. Imag.*, vol. 10, pp. 629–637, Dec. 1991.

[6] H. Eggers and P. Boesiger, "Iterative ΔB_0 and T_2^* correction for radial multi-gradient-echo imaging," in *Proc. ISMRM*, p. 348, 2004.

[7] D. Mentrup and H. Eggers, "Signal decay correction in 2D ultra-short echo time imaging," *Magnetic Resonance Materials in Physics, Biology and Medicine*, 2006.

[8] V. Olafsson, J. A. Fessler, and D. C. Noll, "Dynamic update of R_2^* and field map in fMRI," in *Proc. ISMRM*, p. 45, 2004.

[9] D. B. Twieg, "Parsing local signal evolution directly from a single-shot MRI signal: A new approach for fMRI," *Magn. Reson. Med.*, vol. 50, pp. 1043–1052, 2003.

[10] B. Sutton, D. Noll, and J. Fessler, "Dynamic field map estimation using a spiral-in / spiral-out acquisition," *Magn. Reson. Med.*, vol. 51, pp. 1194–1204, 2004.

[11] —, "Fast, iterative image reconstruction for MRI in the presence of field inhomogeneities," *IEEE Trans. Med. Imag.*, vol. 22, pp. 178–188, Feb. 2003.

[12] H. Eggers, T. Knopp, and D. Potts, "Field inhomogeneity correction based on gridding reconstruction for magnetic resonance imaging," *IEEE Trans. Med. Imag.*, vol. 26, pp. 374 – 384, 2007.

[13] G. H. Golub and C. F. van Loan, *Matrix Computations*, 2nd ed. Johns Hopkins University Press, 1993.

[14] M. Hestenes and E. Stiefel, "Methods of conjugate gradients for solving linear systems," *J. Res. Nat. Bur. Standards*, vol. 49, pp. 409 – 436, 1952.

[15] T. Knopp, S. Kunis, and D. Potts, "A note on the iterative MRI reconstruction from nonuniform k-space data," *Int. J. Biomed. Imag.*, vol. 2007, pp. Article ID 24 727, 9 pages, 2007.

[16] A. Dutt and V. Rokhlin, "Fast Fourier transforms for nonequispaced data," *SIAM J. Sci. Stat. Comput.*, vol. 14, pp. 1368 – 1393, 1993.

[17] H. Schomberg, "Off-resonance correction of MR images," *IEEE Trans. Med. Imag.*, vol. 18, pp. 481 – 495, 1999.

[18] J. F. Kaiser, *Digital Filters*, in System Analysis by Digital Computer, F. F. Kuo and J. F. Kaiser, Ed. Wiley, 1966.

[19] J. A. Nelder and R. Mead, "A simplex method for function minimization," *Comput. J.*, vol. 7, pp. 308–313, 1965.

[20] D. Marquardt, "An algorithm for least-squares estimation of nonlinear parameters," *J. Soc. Indust. Appl. Math.*, vol. 11, pp. 431–441, 1963.

[21] D. Comaniciu and P. Meer, "Mean shift: A robust approach toward feature space analysis," *IEEE Trans. Pattern Anal. Mach. Intell.*, vol. 24, pp. 603 – 619, 2002.

[22] R. D. Hoge, R. K. Kwan, and G. B. Pike, "Density compensation functions for spiral MRI," *Magn. Reson. Med.*, vol. 38, pp. 117–128, Jul 1997.